15th IFK
Proc. of the 15th International Fluid Power Conference <Symposium/Conference>
<DOI>

Influence of surface structuring on the hydrostatic and hydrodynamic pressure distribution of slipper sealing lands

Svenja Horn, Jürgen Weber

Institute of Mechatronic Engineering, TU Dresden, svenja.horn@tu-dresden.de

Abstract.

Modern operating conditions and upcoming lead-free material regulations challenge the tribological performance of axial piston pumps, particularly at low speeds where hydrodynamic support is weak. While meso-structures on slipper surfaces have shown practical success, a fundamental understanding of their working principles is lacking. This paper presents a systematic analysis of how specific geometric parameters of step and parabolic structures influence the hydrostatic and hydrodynamic performance of the slipper-swashplate interface. Simplified analytical models based on the Reynolds equation are used to evaluate the impact on hydrostatic balance and hydrodynamic tilting moments. The findings are qualitatively compared with results from a comprehensive Caspar FSTI simulation. Results show that a smaller gap height at the inner radius reduces the hydrostatic balance but generates a stabilizing tilting moment in the direction of movement. A reduced gap at the outer side of the sealing land by contrast, increases the hydrostatic balance but at the cost of a destabilizing negative tilting moment. The analytical trends are confirmed by the dynamic simulations, providing a foundational understanding for designing structured surfaces to improve pump reliability and efficiency.

Keywords. Surface structures, slipper geometry, axial piston pump, tribology

1. INTRODUCTION

New operating ranges motivated by electrification, start-stop applications or speed-variable drives challenge traditional hydraulic machines with respect to mixed friction conditions, low swash plate angles and partial load operation. At these critical conditions, the pumps are exposed to reduced hydrodynamic pressure in the lubricating gaps, leading to increased friction losses, wear, and a higher likelihood of failures. Traditionally, to ensure good run-in behavior and satisfactory dry-running performance under mixed friction, a combination of leaded bronze or brass and steel materials has been used. However, future EU regulations will prohibit the use of lead-containing materials. In light of these upcoming restrictions, it becomes imperative to find new solutions to withstand the harsh operating conditions without the use of lead-containing metals.

The main difficulty centers the lubrication gaps of the pump's rotating group. Illustration 3 and 4 in Figure 1.1 explain the principal correlation between surface geometry and power losses for the slipper / swash plate interface. There are two forces, that mainly determine the gap height between slipper and swashplate. The piston force F_{SK} from the pressure in the displacement chamber and the opposed lift force F_{fz} due to the pressure distribution of the fluid film lubrication in the gap. A trade-off arises due to the conflicting requirements on the gap height to allow good bearing properties while reducing leakage at the same time. Figure 1.1-4 shows the optimization problem between leakage and friction depending on the gap height. The larger the gap, the higher the leakage, with a simultaneous decrease in friction losses. As the curves have different optima depending on the operating point and design, there is an optimum slipper design for each operating point.

This optimization challenge is addressed by the design of meso-structures. Meso-structures are surface designs that exhibit small changes in height (in the µm range) over larger distances (in the mm range). The principal mechanism of surface structuring on power losses is illustrated in Figure 1.1, using results of chapter 4. Meso-structures allow to change the pressure field in the gap in a targeted way and thus to build up additional hydrodynamics, depicted exemplary for a step structure in Figure 1.1-1 and Figure 1.1-2. This again changes the balance of forces and moments (Figure 1.1-3), which ultimately determines the gap height and slipper's micro motion and associated power losses (Figure 1.1-4).

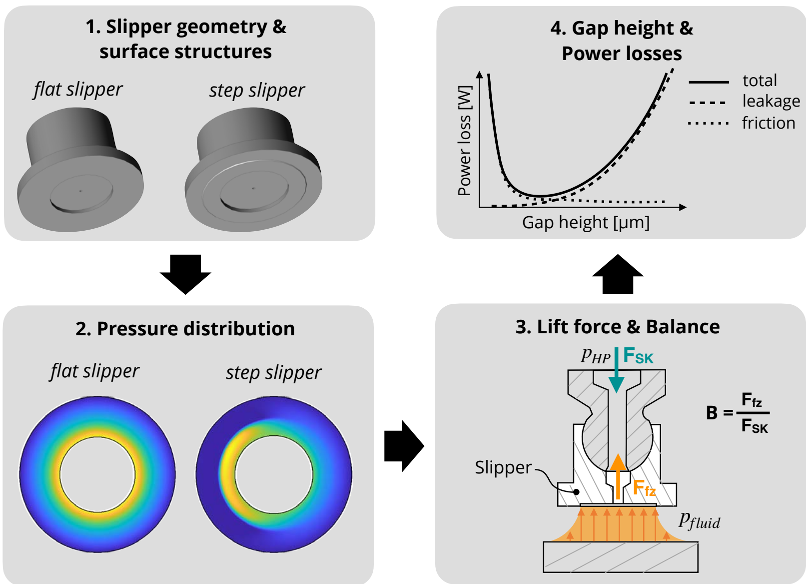

Figure 1.1. Principal mechanism of surface structuring on power losses

Our earlier publications have demonstrated the practical success of these structured surfaces. Several structures on the slipper sealing land have been investigated and optimized using the pump simulation software Caspar FSTI in [1]. The two most promising designs from simulation were manufactured and validated on a dedicated pump test-rig, showing almost no wear [2] and an increase in efficiency for low speeds, low pressures as well as partial load conditions [3]. They were further investigated on the tribometer in [4] and [5] being exposed to extreme thermal conditions and different pressure pulsations.

While these results confirm the significant potential of meso-structures, a fundamental understanding of how specific geometric parameters influence the underlying hydrostatic and hydrodynamic mechanisms is still lacking. The objective of this work is to draw a systematic analysis to bridge this knowledge gap, which will not only enable more efficient design of new slipper geometries but also describes the effect of wear-induced surface changes. The findings are expected to be transferrable to other bearings within axial piston pumps and also to a broader class of plain bearings.

Chapter 3 establishes the theoretical foundation for pressure build-up in lubricating gaps, based on the Reynolds equation, and introduces the two selected surface structures for analysis. In chapter 4, the influence of key geometric parameters on both the hydrostatic balance and the hydrodynamic tilting moments are investigated in detail for each design. The findings for the first structure are also compared with results from a comprehensive simulation to contextualize the analytical approach in chapter 5. The paper concludes with a summary of the key findings and their implications for the design and optimization of tribological interfaces in axial piston pumps.

2. LITERATURE

The performance of the slipper-swashplate interface has been a subject of extensive research, with a particular focus on the influence of the slipper's surface geometry on the lubricating film. Early analytical investigations by Hooke established that a convex slipper profile is crucial for ensuring stable fluid film lubrication [6]. This finding was later reinforced by Borghi et al., who used simulations to show that an initially flat slipper is inherently unstable and will eventually wear into a convex shape to achieve stable operation [7]. However, the ideal profile is not straightforward. Manring, for instance, found that while a linear concave profile could increase load-carrying capacity, it came at the cost of higher leakage and power loss. His work further revealed that profile deformations have a greater impact on flow rate than on load-carrying capacity, highlighting the complex trade-offs inherent in slipper design [8].

More recent studies employing Elastohydrodynamic (EHD) models have provided deeper insights into the role of deformation. Hashemi et al. developed a "tribo-slipper-pump" test rig and showed through both measurement and simulation that a slightly concave slipper can deform elastically under high pressure to form a convex shape, thereby improving its hydrodynamic characteristics [9]. This underscores the importance of considering material deformation in any realistic analysis. Beyond general surface profiles, specific geometric structures have been proposed to actively manipulate the pressure field. A notable example of using a micro-step is found in the patent US 5,983,781 by Ivantysyn, from 1999 [10]. It is relevant to note that this patent has since expired, placing the described invention in the public domain. The patent describes a shallow recess at the inner diameter of the sealing land, which is designed to create a self-adjusting load-bearing capacity that changes with the gap height [10]. While the patent focuses on this specific self-adjusting mechanism, the present work undertakes a broader, systematic analysis of such step structures. It investigates the fundamental effects of varying key parameters, including step height and position, on the hydrostatic and hydrodynamic performance. This allows for a more comprehensive understanding of the design trade-offs, building on the concepts introduced in earlier work. Another promising approach involves sinusoidal or wave-like structures. Baker and Ivantysyn investigated sinusoidal meso-structures on the sealing land of a valve plate, using simulation to optimize the wave's frequency, amplitude, and phase [11], [12]. The most promising design was manufactured and tested, demonstrating an increase in the total pump efficiency of up to 10 % at low displacement and pressure [11]. While this technology was patented in the United States in 2009, it was not extended elsewhere, making the application and further development freely available in other markets, including Europe [13]. The success of this wave profile on the valve plate provides a strong motivation for investigating a similar radial wave structure on the slipper surface, as is done in the previous studies.

Other approaches include surface texturing. Ye et al. used an EHD model to identify an optimal dimple area density and depth-to-diameter ratio to maximize load-carrying capacity [14]. Similarly, Wang et al. simulated micro-textures with varying dimple shapes and depths, also finding improvements in load-carrying capabilities and friction losses, though these results were not experimentally validated [15].

A significant contribution to surface optimization on the slipper sealing land was made by Darbani et al., who proposed an optimized convex shape derived from typical wear profiles [16]. Their work aimed to minimize total energy loss across various operating conditions, reporting a theoretical efficiency improvement of around 51%, mainly decreasing friction losses at high speeds [16]. However, the study has limitations: the results were not experimentally validated, and crucial geometric data such as the slipper balance factor were whether provided nor changed, making the findings difficult to transfer or compare directly. Despite these gaps, the promising results from this optimization approach motivate the inclusion of a similar convex profile in the present analysis. More recently, Mo et al. also analyzed the influence of different convex wear profiles on lubrication performance, though the analysis was limited to a single operating point and did not include an optimization perspective [17].

A key challenge in analyzing these complex interactions is to distinguish the contributions of hydrostatic and hydrodynamic effects. A recent methodological advancement by Ernst and Vacca demonstrated a technique for separating the hydrostatic and hydrodynamic force components from the simulated pressure distribution [18]. Their findings revealed that while the load is primarily carried hydrostatically, the hydrodynamic component can account for over 20 % of the total lift under certain conditions, playing a critical role in balancing the system [18]. This approach of separately analyzing hydrostatic and hydrodynamic effects is adopted in the present work to provide a fundamental understanding of how specific geometric parameters influence each mechanism.

3. THEORETICAL BACKGROUND AND METHODOLOGY

3.1. Pressure build-up in small lubricating gaps

The pressure distribution within the lubrication gaps of axial piston pumps determines the forces and moments acting on the components and can be described by the Reynolds equation, first derived from the Navier Stokes momentum and continuity equations by

Osborne Reynolds in 1886 [19]. Considering a very small fluid gap height in the range of micrometer together with a large gap length in the range of millimeter, as it is the case for the lubricating gaps in axial piston pumps, several assumptions can be made, that simplify the complex Navier Stokes equation. These include assuming constant pressure over the fluid film thickness $\partial p/dz = 0$, neglecting inertial and body forces as they are very small compared to the viscous and pressure forces, and considering the lubricant to be a Newtonian fluid, where shear stress is proportional to the shear rate. For the analytical approach in this work, the fluid is further assumed to be incompressible and of constant viscosity. Under these assumptions, the generalized Reynolds equation is given by [18]

$$\begin{aligned} &\underbrace{\frac{\partial}{\partial x}\left(\frac{\rho h^3}{12\mu}\frac{\partial p}{\partial x}\right) + \frac{\partial}{\partial y}\left(\frac{\rho h^3}{12\mu}\frac{\partial p}{\partial y}\right)}_{\text{Poiseuille}} = \underbrace{\frac{\partial}{\partial x}\left(\frac{\rho h(u_\mathrm{a} + u_\mathrm{b})}{2}\right) + \frac{\partial}{\partial y}\left(\frac{\rho h(v_\mathrm{a} + v_\mathrm{b})}{2}\right)}_{\text{Couette}} \\ &\underbrace{+ \rho\left(w_\mathrm{a} - w_\mathrm{b} - u_\mathrm{a}\frac{\partial h}{\partial x} - v_\mathrm{a}\frac{\partial h}{\partial y}\right)}_{\text{Squeeze}} + \underbrace{h\frac{\partial \rho}{\partial t}}_{\text{Expansion}} . \end{aligned} \tag{3.1}$$

The equation consists of several terms that represent different physical effects. The *Poiseuille* term describes the flow rates due to pressure gradients and is used to calculate the hydrostatic pressure field in the gap. The *Couette* term describes the hydrodynamic pressure build up due to the relative sliding motion of the surfaces. This hydrodynamic effect is primarily generated by a "physical wedge," where a converging geometry in the direction of motion creates positive pressure [20]. The squeeze term accounts for the cushioning effect when surfaces move towards or away from each other, generating pressure in response to a changing film thickness. The local expansion term describes the impact of mechanical or thermal deformations on the fluid film thickness. This paper focuses on the hydrostatic (Poiseuille) and hydrodynamic (Couette) effects to understand the fundamental influence of surface geometry.

A key metric for evaluating the hydrostatic design is the balance factor, calculated by dividing the hydrostatic lift force by the opposing piston force. A balance of 100 % indicates that the forces are in equilibrium. In industrial practice, slippers are often designed with a balance around 90 % to allow for additional hydrodynamic lift at higher speeds. However, this under-balance can lead to high friction and wear during start-up and at low speeds when hydrodynamic effects are weak. Conversely, a balance factor near or above 100 % can ensure separation but may lead to increased leakage losses.

The primary mechanism for generating hydrodynamic pressure is the wedge effect, which can be created by a tilted surface or a geometric feature like a step, as illustrated in Figure 3.1. The magnitude of hydrodynamic pressure generated is dependent on the ratio between the minimum gap height and the height of the geometric feature (i.e., step or inclination height). For the specific case of a parallel-step bearing, an optimal configuration that maximizes hydrodynamic lift was first derived by Lord Rayleigh [21]. As presented in detail in [20], this optimum is defined by the following dimensionless parameters for the step height ratio, H_0, and the step position ratio, n_s:

$$H_0 = \frac{h_0}{s_h} = 1.155,\ n_s = 0.7182. \tag{3.2}$$

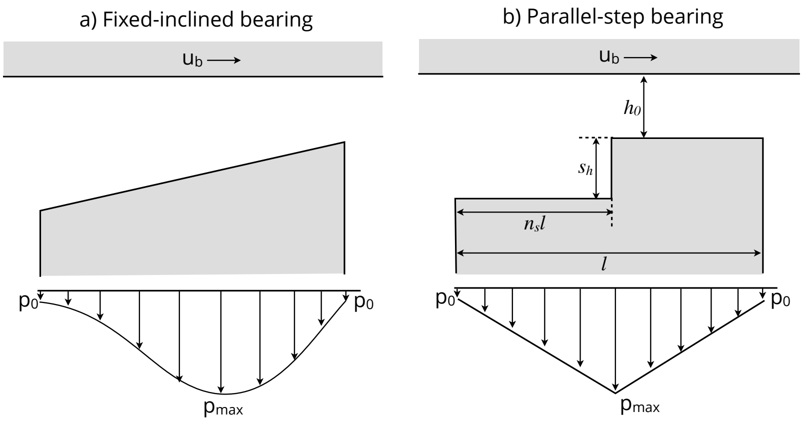

Figure 3.1.Comparison of pressure profiles of fixed inclined bearing (a) and parallel-step bearing (b)

3.2. Selected surface structures

The left plot in Figure 3.2 illustrates the slipper geometry, with the most important parameters the pocket diameter d_{inG}, the sealing land outer diameter d_{outG} and the gap height h. To further investigate the influence of surface structures on the hydrostatic and hydrodynamic pressure build-up, two representative surface designs (see Figure 3.2) from literature were selected for detailed analysis:

- **Design a):** A step structure several micrometers in height, resulting in a reduced gap at the inner land of the slipper surface. This concept is derived from classical step slider bearing designs and, compared to the other structures, offers significant advantages in terms of manufacturing simplicity.
- **Design b):** A parabolic surface profile, which mimics the typical run-in wear pattern of the slipper surface. This profile arises due to thermal and pressure-induced deformation, leading to abrasion at the inner radius, and tilting-induced wear at the outer radius. Darbani optimized this design using the CASPAR simulation environment [16]. However, no manufacturing or experimental validation has been reported to date.

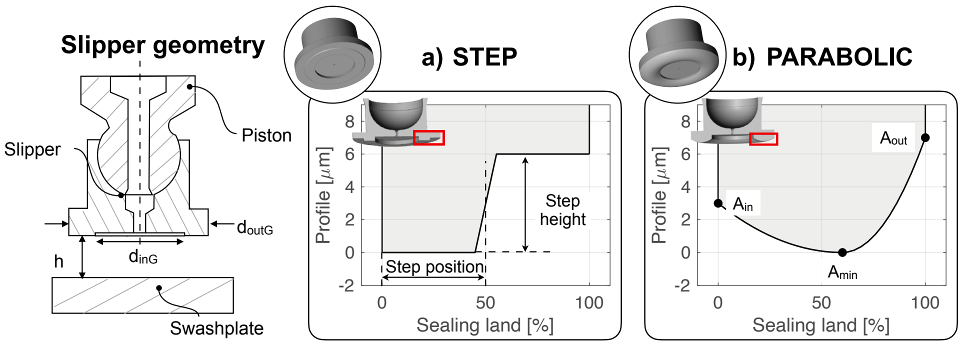

Figure 3.2. Slipper geometry and design spaces of two different surface structures

These surface structures were chosen to represent a spectrum of complexity and manufacturability, as well as to capture different mechanisms of pressure generation and wear compensation. In the following, their impact on the pressure build-up in the lubricating gap will be systematically analyzed and compared.

3.3. Methodology

In the following, the influence of the design parameters on the hydrostatic and hydrodynamic lift force is investigated. In order to take into account the later dimensions of the test pump at this point and at the same time remaining company-neutral, the outer diameter d_{outG} of the slipper is set to 29.6 mm, which is an average value of industrial slipper outer diameters with a 21 mm piston. To directly see the influence of the surface structure, the inner radius is calculated such that a balance of 100 % is achieved. A gap height of h=20 µm during high pressure stroke is set to calculate the hydrostatic and hydrodynamic pressure build-up. To quantify the hydrostatic forces and hydrodynamic moments based on the principles of the Reynolds equation, simplified analytical methods are employed. Bergada detailly derives the calculation of the lift force of a multi-land slipper design in [22]. His approach is transferable to micro-structured sealing lands, as it discretizes the radial gap height *h(r)*, using the following formula to calculate the lift force F_{fz}:

$$F_{fz} = p_{\text{in}} \cdot \pi \cdot \left[\frac{\sum_{i=1}^{i=n} \frac{1}{h_i^3} \cdot \frac{r_{i+1}^2 - r_i^2}{2}}{\sum_{i=1}^{i=n} \frac{1}{h_i^3} \cdot \ln\left(\frac{r_{k+1}}{r_k}\right)} - r_1^2 \right] \tag{3.3}$$

This calculation accounts for the modified pressure profile caused by the structure. It is important to distinguish this from a conventional balance calculation based solely on the fixed pocket and sealing land diameters, which would not capture the influence of the meso-structure.

For the analysis of hydrodynamic effects, a simplified 1D analytical model, as implemented by Knoll is used [23]. This approach solves a one-dimensional form of the Reynolds equation (Equation (3.4), assuming the slipper sealing land is an infinitely wide bearing. This reduces the problem to the direction of motion (x_G) and allows for rapid evaluation of the pressure profile *p(x)* generated by the Couette term.

$$\frac{\partial}{\partial x_G}\left(h^3 \frac{\partial p}{\partial x_G}\right) = 6u\mu \frac{\partial h}{\partial x_G} \tag{3.4}$$

The resulting 1D pressure profile p(x) is then integrated across the sealing land width to calculate the hydrodynamic tilting moment M_y around the y_G-axis, providing a direct measure of the structure's tendency to generate a stabilizing or destabilizing pitch:

$$M_y = \int p(x) \cdot x \, dx. \tag{3.5}$$

4. RESULTS

This chapter presents the influence of key geometric parameters on the hydrostatic balance and the hydrodynamic tilting moments first for the step and second for the parabolic design. The findings for the step structure are further compared with results from a comprehensive simulation to contextualize the analytical approach.

4.1. a) Step structure

4.1.1. Influence on hydrostatic pressure and balance

The initial investigation focuses on the examination of the impact of the step design parameters, specifically the step height and position, on the hydrostatic. Figure 4.1 (left) shows, as a dashed black line, the typical logarithmic pressure drop across the sealing land for a flat, unstructured slipper with a balance of 100 % (pocket diameter of 14.4 mm) at a pocket pressure of 100 bar and a gap height of 20 µm (design *a3*). The colored lines represent three example pressure distributions for a step located in the middle of the sealing land, with varying step heights. Designs *a1* and *a2* feature a step with a reduced gap height at the inner radius, elevated by 6 µm and 3 µm, respectively. In contrast, design *a4* has a 3 µm-high step at the outer radius, reducing the gap height there. A smaller gap at the inner radius causes a more rapid pressure drop in the inner region, resulting in a lower lift force and thus a reduced balance. Conversely, a reduced gap at the outer radius (*a4*) leads to a slower pressure drop in that area, increasing the hydrostatic force and balance. The right-hand plot in Figure 4.1 shows the resulting balance as a function of step height and step position, with the four designs *a1*–*a4* indicated.

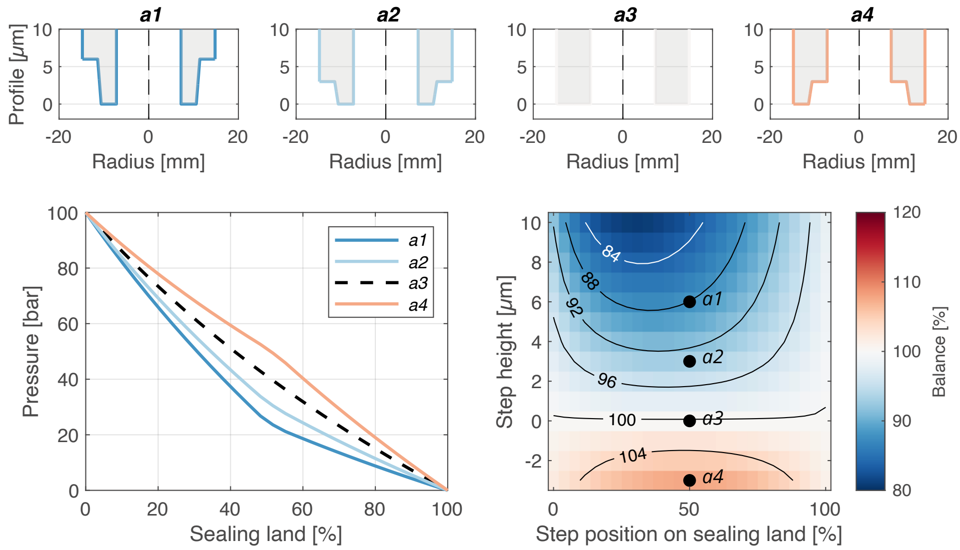

Figure 4.1. Sealing land Pressure drop over sealing land for different surface structured designs (*a1, a2, a4*) in comparison to an unstructured slipper *a3* (left) and balance for different step heights and step positions (right)

Figure 4.2 left shows that the gap height for an unstructured flat slipper (design *a3*) has no impact on the balance, while it strongly changes the balance for the structured slippers (*a1, a2* and *a4*) especially for smaller gap heights below 10 µm. It is particularly noticeable that the designs *a1* and *a2* with a smaller gap at the inner ring have less lift for smaller gap heights, dropping below 80 % for a 3 µm gap height. Design *a4* on the other side exhibits a balance of over 140 % for a 3 µm gap height providing extra lift in case of critical mixed friction conditions. All designs have a pocket radius of 7.2 mm.

Figure 4.2 right illustrates the balance for different pocket diameters ranging from 7-8 mm and gap heights from 3-30 µm for the structured design *a1*. While the pocket diameter has a linear impact on the balance value, the impact of the gap height on the balance value is significantly higher at lower gap heights.

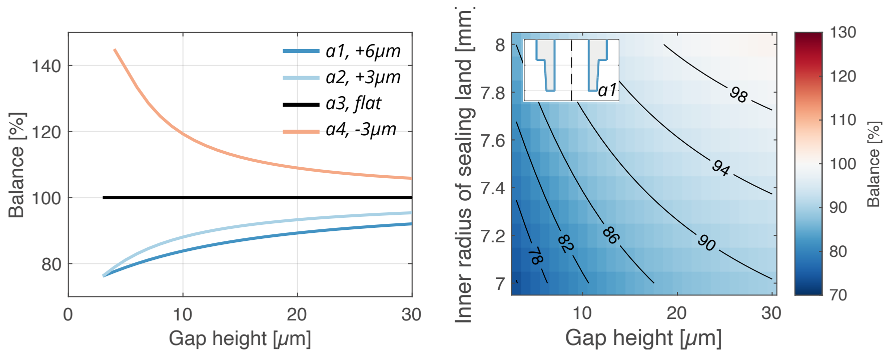

Figure 4.2. Influence of gap height on balance for different designs *a1*-*a4* (left) and balance for different pocket diameter and gap height combinations for design *a1* (right)

4.1.2. Influence on hydrodynamic lift and tilting moment

Figure 4.3 (top) shows the radial cross-sectional profiles of the three designs *a1, a2*, and *a4*. The lower part of the figure presents a qualitative representation of the resulting hydrodynamic pressure distribution, calculated at a rotational speed of 500 rpm and an external pressure of 0 bar without any slipper tilt. The direction of movement *u* is defined to the right. The triangular hydrodynamic pressure build-up caused by the step corresponds to that of a parallel-step bearing, as shown in Figure 3.1.

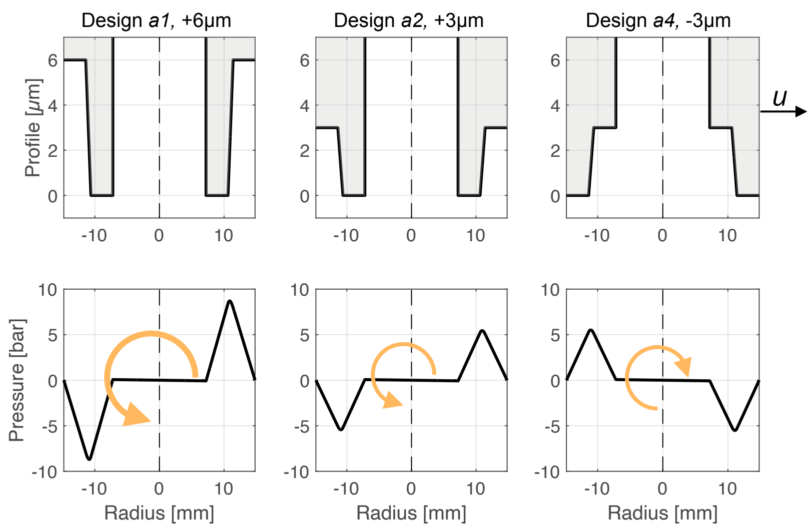

Figure 4.3. Radial cross-sectional profiles of designs *a1*, *a2*, and *a4* (top) and corresponding qualitative hydrodynamic pressure distribution at 500 rpm (bottom)

A diverging gap in the direction of motion leads to a positive pressure build-up, whereas a converging gap results in a negative pressure. While negative pressures cannot occur in reality and are merely the result of a mathematical solution under the given boundary conditions, the simplified example nonetheless illustrates the effect induced by the step. In a physical system, a liquid cannot sustain significant tension, and the pressure will not drop below the fluid's cavitation pressure. A smaller gap at the inner radius (as for *a1* and *a2*) causes an uneven hydrodynamic pressure distribution due to the wedge effect in the flow direction, resulting into a positive tilting moment, causing the slipper to pitch upward and align itself in a way that promotes further hydrodynamic pressure build-up. In contrast, a step in the opposite direction as for design *a4* induces a negative tilting moment, which may cause the slipper to "sink" or lose its load-carrying capacity.

Figure 4.4 illustrates the tilting moments generated by the step structure and calculated with a 20 µm gap height and a dynamic viscosity of $\eta = 0.0705$ Pas. Positioning the step near the inner radius results in a positive tilting moment, which acts to pitch the slipper upward and enhance hydrodynamic support. In contrast, a step near the outer radius creates a negative, potentially destabilizing moment. This fundamental behavior aligns with the principles first established by Lord Rayleigh for ideal parallel-step bearings, which predict an optimal configuration for maximizing lift (refer to formula (3.2)) [20].

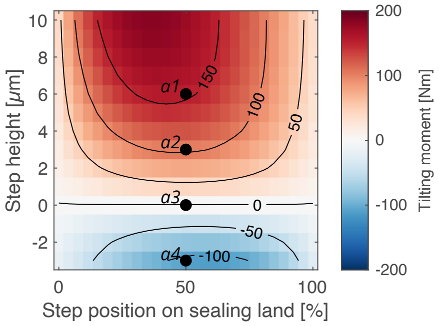

Figure 4.4. Tilting moment generated by hydrodynamic pressure for various step heights and step positions on the sealing land

The results in Figure 4.4 show that for the slipper geometry in this study, the maximum positive tilting moment is found for a step position of approximately 40 % of the sealing land width. This is in the same region as, though slightly outward from, the theoretical optimum of ~30 % predicted by Rayleigh's theory. Similarly, the optimal step height of around 10 µm (for a 20 µm gap) is in the same order of magnitude as the classical prediction, confirming the validity of the general principle.

4.2. b) Parabolic structure

4.2.1. Influence on hydrostatic pressure and balance

The parabolic design is showing a typical wear profile of the slipper sealing land. Starting with the influence of the parabolic design parameters A_{in}, A_{out} and A_{min} on the hydrostatic behavior, Figure 4.5 (left) shows the pressure profiles across the sealing land. The reference design *b3*, without any structural modification, is shown as a dashed line. The colored curves illustrate four modified designs: *b1* and *b2* feature a parabolic recess at the outer radius with depths of 10 µm and 5 µm respectively, that can for example be caused by slipper tilting. *b4* and *b5* have a recess at the inner radius with the same depths and can be produced by convex deformation of the slipper surface. As already observed in the step design, material removal at the outer radius (*b1, b2*) causes a reduction in pressure compared to the unprofiled reference, whereas a recess at the inner radius (*b4, b5*) leads to an increase in pressure. This behavior corresponds to a decrease or increase in the hydrostatic balance of the slipper, as shown in the right plot of Figure 4.5. Here, the design space covers also quadratic designs with a recess at both, the outer and inner radius, with a curve minimum at A_{min}=50 %.

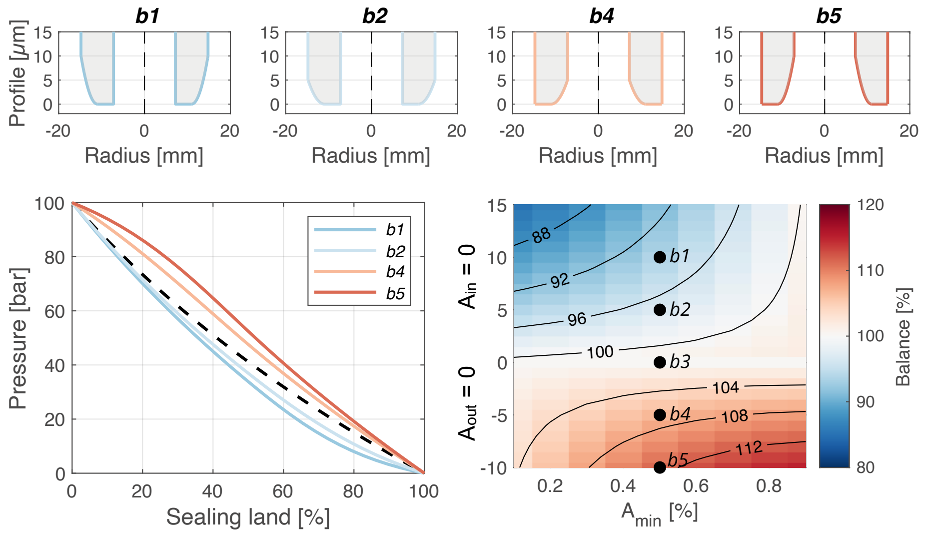

Figure 4.5. Hydrostatic pressure drop over the sealing land for different parabolic designs *b1-b5* (left) and hydrostatic balance map for different combinations of the parameters A_{in} and A_{out}, with different curve minimums A_{min} (right)

Further balance maps with different curve minimums at 20, 50 and 80 % are presented in Figure 4.6. A shift of the curve minimum to the inner radius reduces the balance while a shift to the outer radius increases the balance, aligning with the trends of the step design.

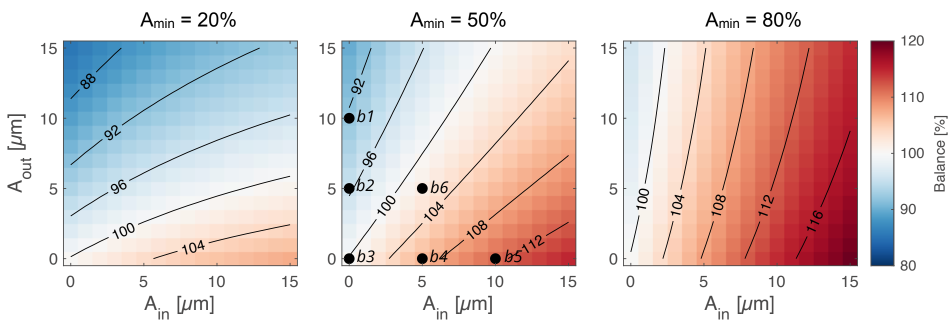

Figure 4.6. Influence of quadratic curve minimum A_{min} on balance for different combinations of A_{in} and A_{out}

4.2.2. Influence on hydrodynamic lift and tilting moment

In Figure 4.7 on the top, the radial cross-sectional profiles of the three designs *b2*, *b6* and *b4* are drawn in more detail. Below, the corresponding qualitative hydrodynamic pressure distributions are calculated at 20 µm gap height, 500 rpm and no slipper tilt. Design *b2* and *b4* produce the same hydrodynamic pressure however mirrored such that wear at the outer radius results in a positive tilting moment, while wear at the inner radius produces a negative tilting moment. A recess at the inner and outer radius (*b6*) varies the hydrodynamic pressure according to the positive and negatives edges of the profile. In total, a slightly positive tilting moment result.

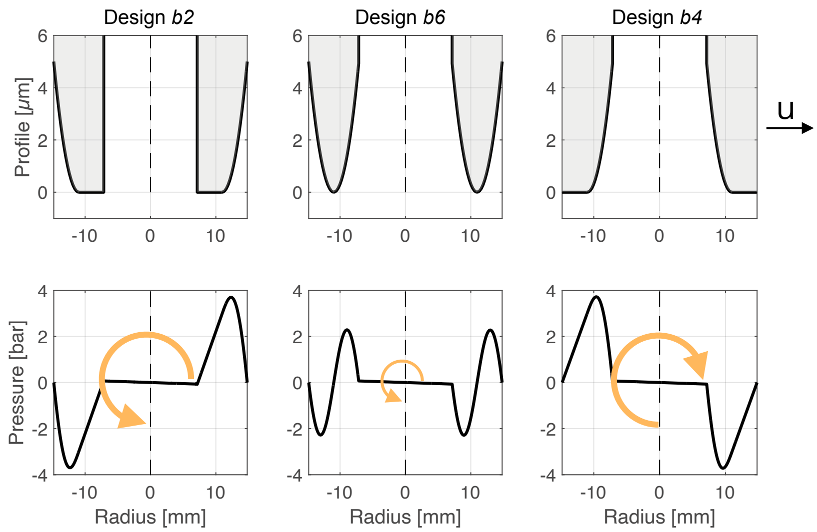

Figure 4.7. Radial cross-sectional profiles of designs *b2*, *b6* and *b4* (top); corresponding qualitative hydrodynamic pressure distribution at 500 rpm (bottom)

Figure 4.8 summarizes the tilting moments of a wide range of combinations of the parabolic design parameters A_{in} and A_{out} for three different values of A_{min}. The more at the inner radius, the curve minimum exists, the more the recess at the outer radius dominates resulting into a broader area of a positive tilting moment (compare the large red area in the left plot with the large blue area in the right plot).

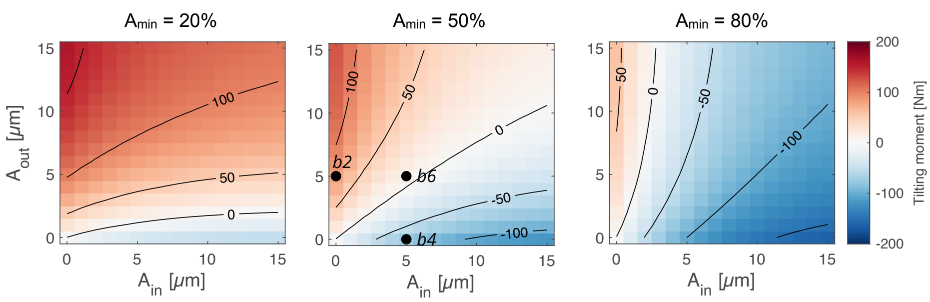

Figure 4.8. Tilting moment generated by hydrodynamic pressure for different quadratic curve minimums A_{min} over A_{in} and A_{out}

5. Comparison with simplified simulation results

To validate the fundamental trends observed in the simplified analytical model, a comparison is made with the comprehensive FSTI CASPAR simulation. This step is necessary to confirm that the basic physical effects predicted by the static, analytical approach hold true within a more complex simulation that seeks a system's force and moment equilibrium. However, a direct quantitative validation presents a methodological challenge. The analytical approach calculates forces for a predefined, fixed gap height, producing maps of force balances versus geometry. In contrast, the FSTI simulation is designed to find the system's equilibrium state. It iteratively adjusts the gap height and slipper tilt until the forces and moments precisely balance the external loads (e.g., the piston force). Consequently, the simulation's primary output is the final equilibrium gap height for a given operating point, not a map of forces at various non-equilibrium gap heights.

5.1. Simulation setup and parameter selection

To create a qualitative comparison despite this fundamental difference, several steps were taken. First, the FSTI simulation was simplified to more closely match the assumptions of the analytical model by deactivating squeeze effects and deformations. Second, a key challenge was identifying simulation parameters that yielded stable, converged results with physically meaningful gap heights for all designs. Many initial simulations failed to converge. Therefore, only a smaller selection of the step designs *a1-a4* is chosen for the comparison. Runs with a smaller pocket radius (7.2 mm, as used in the analytical study) resulted in predicted gap heights that were too small, particularly for design *a1*. This approached a mixed-friction regime that the simulation cannot accurately depict. Consequently, a larger pocket radius of 8.2 mm was selected. At an operating condition of 100 bar and 500 rpm, this configuration produced reasonable and comparable equilibrium gap heights.

Figure 5.1 (left) illustrates the slipper coordinate system, in which the direction of movement is defined by x_G and the velocity by u. The high- and low-pressure regions are marked in red and blue and the angle of rotation is defined by ϕ, which ranges from 0 to 360°.

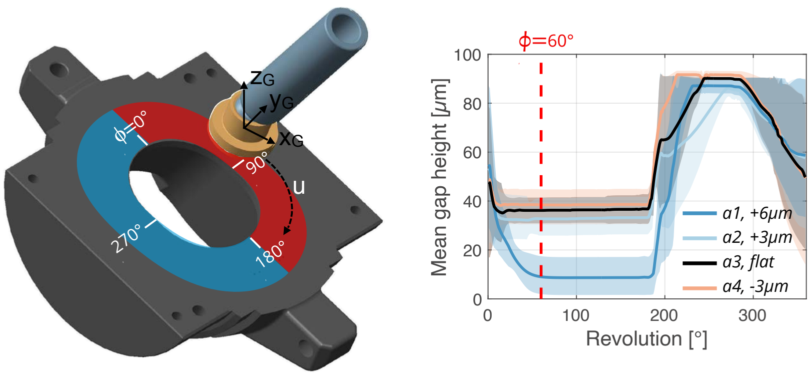

Figure 5.1. Mean gap height over one pump revolution for all designs *a1-a4* with shaded regions indicate min-max range (right)

Figure 5.1 (right) presents the resulting mean gap heights for designs *a1*-*a4* over one pump revolution, with shaded regions indicating the spread between minimum and maximum values. As predicted by the analytical balance calculations, design *a1*, which has the lowest hydrostatic balance, also exhibits the lowest minimum gap heights in the simulation. The maximum value of the curves during the low-pressure phase is due to the slipper hold-down mechanism, which limits the maximum gap height to 90 µm. The red dotted line indicates a rotation angle of 60°, at which point gap heights and pressure fields are evaluated further.

The next two paragraphs analyze the influence of the meso-structures on the hydrostatic and hydrodynamic pressure build-up in isolation. As the outputs of the FSTI simulation comprise the results of the total Reynolds equation, it is necessary to separate the hydrostatic and hydrodynamic components of the pressure field from the final simulation outputs. To achieve this, a post-processing script was used [23], which implements the methodology for pressure component separation proposed by Ernst and Vacca [18]. This method first uses the results from the full fluid-structure interaction simulation (total pressure p_{tot} and equilibrium gap height). It then resolves the Reynolds equation using only the hydrostatic (Poiseuille) term, treating the final gap height and fluid properties as known constants. The resulting pressure field is the pure hydrostatic component (p_s), and the hydrodynamic component (p_d) is subsequently found by subtraction: $p_d = p_{tot} - p_s$ [18].

Figure 5.2 illustrates the results of the pressure separation for design *a2* at 60° during the high-pressure phase. The gap height distribution (left) reveals the slipper's backward tilt, which directly influences the pressure fields. The hydrostatic component (middle) exhibits the expected radial symmetry, whereas the hydrodynamic component (right) reflects the wedge effect created by the tilt: regions of positive pressure (yellow) form where the gap converges, and sub-ambient pressure (blue) develops at the location of smallest gap height. It should be noted that the negative pressure values are a mathematical result of the separation methodology. In reality, the fluid cannot sustain such tensions and would cavitate; however, this does not affect the validity of the qualitative trends. The red dotted line in b) marks the path analyzed in Figure 5.3.

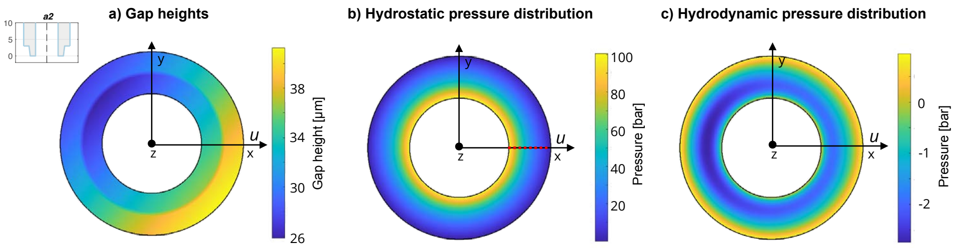

Figure 5.2. Gap height (left), hydrostatic (middle) and hydrodynamic (right) pressure fields for design *a2* at 60°; the red dotted line marks the path analyzed in Figure 5.3.

5.2. Influence on hydrostatic pressure and balance

Figure 5.3 compares the simulated (left) and analytically calculated (right) pressure drop across the leading sealing land for all four designs at $\phi = 60°$. Unlike in chapter 4, the analytical model employs the same pocket diameter of 8.2 mm as the simulation and uses the different mean gap heights at $\phi = 60°$ from Figure 5.1 as inputs. The resulting pressure profiles are qualitatively and apart from minor differences also quantitatively comparable.

Those minor deviations may arise from the pressure component separation methodology [18].

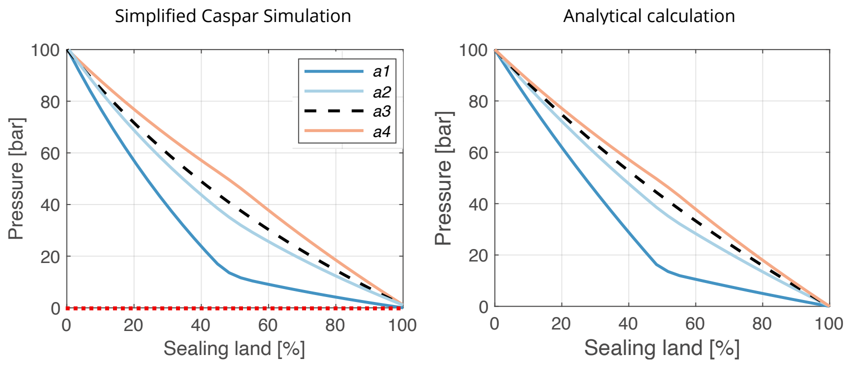

Figure 5.3. Pressure drop over the leading sealing land for all designs *a1-a4* at 60° pump revolution from simulation (left) and analytically calculated (right)

5.3. Influence on hydrodynamic lift and tilting moment

Figure 5.4 displays the respective hydrodynamic pressure fields for designs *a1-a4*, with the resulting tilt axis marked as a dashed line. The opposite tilting moment directions—negative for the outer step (*a4*) versus positive for the inner steps (*a1-a3*)—are clearly visible in the pressure field orientations relative to slipper velocity u. Among designs *a2-a4*, which share similar gap heights, the trend is solely geometry-driven: increasing inner step height leads to a larger positive tilting moment and corresponding tilt axis rotation, aligning with the analytical findings in chapter 4. Design *a1* exhibits a notably stronger hydrodynamic effect due to its much smaller gap height, which amplifies the hydrodynamic lift beyond what the step geometry alone would produce.

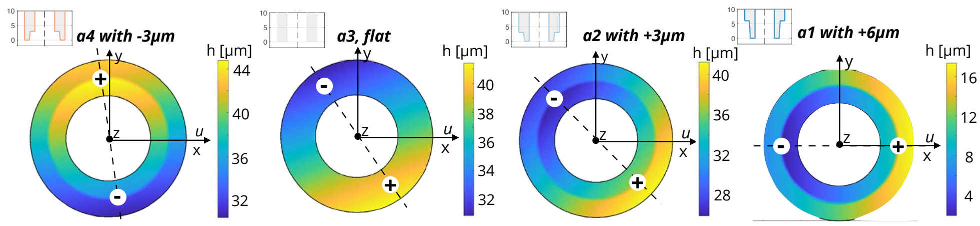

Figure 5.4. Gap height distributions for different step designs *a1-a4* with marked tilt axis at 30° pump revolution during high pressure phase

Figure 5.5 shows the result of this separation for design *a2* at 30° of the pump revolution (high pressure regime), now at an elevated operating pressure of 200 bar (compared to 100 bar in the previous analysis) while maintaining the same speed of 500 rpm. The higher operating pressure was selected because it produces smaller equilibrium gap heights, which in turn amplifies the hydrodynamic pressure generation, making the effect more clearly visible for analysis. The plot on the left displays the isolated hydrodynamic pressure field across the entire slipper land. It clearly shows a region of positive pressure build-up (yellow) and a region of sub-ambient pressure (blue), which is characteristic of the wedge effect. The plot on the right shows the pressure profile along the central x-axis, which is qualitatively similar to the analytical results for a parallel-step bearing (refer to Figure 2.2), confirming that the step is the primary driver of this hydrodynamic effect.

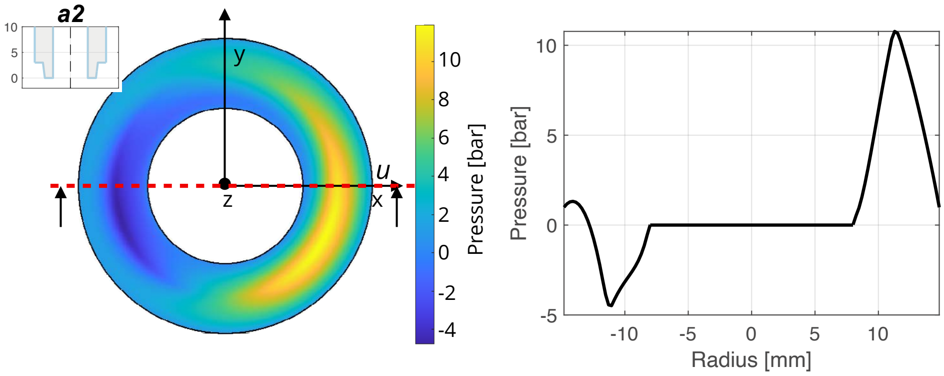

Figure 5.5. Hydrodynamic pressure field at $\phi = 30°$ for design *a2* (left) and hydrodynamic pressure distribution through x-axis (right)

6. DISCUSSION AND OUTLOOK

This study systematically analyzes the influence of meso-structures on the pressure-generating mechanisms in a slipper-swashplate interface, revealing a fundamental trade-off between hydrostatic and hydrodynamic performance. The analytical models and simulation results consistently demonstrate two opposing principles. A reduced gap at the inner side on the sealing land decreases the hydrostatic balance but generates a beneficial positive tilting moment in the direction of motion that promotes hydrodynamic lift. A reduced gap at the outer side of the sealing land by contrast, increases the hydrostatic balance but at the cost of a potentially destabilizing negative tilting moment.

Of particular significance is the observation that the influence of these structures is not constant. The effect on both, hydrostatic balance as well as hydrodynamic lift, becomes more pronounced at smaller gap heights. This non-linear behavior means that the structure's impact is strongest precisely when the slipper operates in critical mixed-friction regimes. This provides a fundamental explanation for the improved reliability of structured surfaces observed in previous experimental work findings provide a clear framework for application-specific design, moving beyond a "one-size-fits-all" approach. For applications dominated by low-speed or start-stop operation where hydrodynamic stability is paramount, a design that guarantees a positive tilting moment is preferable. The associated reduction in hydrostatic balance can be compensated for by adjusting the pocket diameter.

The primary limitation of this analytical study is the neglect of thermo-elastic deformations. As noted in the literature and observed in the FSTI simulations, pressure and temperature-induced deformations can create their own relevant micro-geometry, which may be convex or concave depending on the design and operating point. This deformation can either enhance or counteract the effect of the manufactured structure and has been taken into account for the optimization study in [1].

Beyond the fundamental design trade-offs, the analytical maps presented in this study also provide practical guidance for manufacturing. The contour lines indicate that certain parameters are more tolerant to manufacturing variations than others. For instance, the step position shows relatively flat gradients in the mid-range of the sealing land (approximately 30–60%), meaning that moderate positional deviations have limited impact on the hydrostatic balance. In contrast, the step height exhibits steeper gradients and thus requires tighter manufacturing tolerances to achieve the target performance. This insight is particularly valuable for industrial implementation, as it allows manufacturers to focus precision efforts on the most sensitive parameters while relaxing tolerances where the design is inherently robust.

The findings of this study, particularly the trade-off between hydrostatic balance and hydrodynamic tilting moment, and the non-linear sensitivity of meso-structures at small gap heights, are governed by thin-film lubrication physics and are therefore expected to be transferable to other tribological interfaces in displacement pumps. This includes the valve plate-cylinder block and piston-cylinder bore interfaces in axial piston pumps, as well as the axial thrust bearings in external gear pumps.

ACKNOWLEDGEMENTS

The authors would like to thank Meike Ernst and Andrea Vacca for their foundational methodology on separating hydrostatic and hydrodynamic pressure fields [18], [24]. We are particularly grateful to Meike Ernst for generously providing the original implementation scripts. Access to this sophisticated code greatly facilitated our analysis and saved significant development effort. Special thanks are also extended to Simon Knoll for his diligent work in adapting these scripts for the specific analyses in this study. His development of the 1D analytical model for calculating tilting moments, which formed a significant part of his diploma thesis [23], is also gratefully acknowledged.

REFERENCES

[1] S. Horn, R. Ivantysyn, and J. Weber, "Tribo-optimized lubricating interfaces in hydrostatic pumps with surface shaped slippers," *IFK2022*, 2022.

[2] R. Ivantysyn, S. Horn, and J. Weber, "Design of a Lead-Free Slipper Bearing for Low Speed Axial Piston Pump Applications," *IEEE GFPS 2022*, 2022.

[3] S. Horn, R. Ivantysyn, and J. Weber, "Validated efficiency improvements by implementation of structures on the slipper surface of an axial piston pump," *IEEE GFPS 2022*, 2022.

[4] S. Horn, R. Ivantysyn, and T. Schmidt, "Tribological properties of different slipper designs of an axial piston pump," *Ifk2024*, no. in mm, pp. 1–18, 2024.

[5] S. Horn, T. Schmidt, and P. Kajewski, "Measuring friction of different slipper designs using a hydrostatic tribometer test-rig with pressure pulsation," in *Fachtagung Gesellschaft für Tribologie*, 2025, pp. 1–12.

[6] C. J. Hooke and Y. P. Kakoullis, "The effects of non-flatness on the performance of slippers in axial piston pumps," *Proc. Inst. Mech. Eng. Part C J. Mech. Eng. Sci.*, vol. 197, no. 4, pp. 239–247, 1983, doi: 10.1243/PIME_PROC_1983_197_104_02.

[7] M. Borghi, E. Specchia, and B. Zardin, "Numerical analysis of the dynamic behaviour of axial piston pumps and motors slipper bearings," *SAE Int. J. Passeng. Cars - Mech. Syst.*, vol. 2, no. 1, pp. 1285–1302, 2009, doi: 10.4271/2009-01-1820.

[8] N. D. Manring, R. E. Johnson, and H. P. Cherukuri, “The impact of linear deformations on stationary hydrostatic thrust bearings,” *J. Tribol.*, vol. 124, no. 4, pp. 874–877, 2002, doi: 10.1115/1.1482118.
[9] S. Hashemi, H. Friedrich, L. Bobach, and D. Bartel, “Validation of a thermal elastohydrodynamic multibody dynamics model of the slipper pad by friction force measurement in the axial piston pump,” *Tribol. Int.*, vol. 115, no. May, pp. 319–337, 2017, doi: 10.1016/j.triboint.2017.05.013.
[10] J. Ivantysyn, “Sliding bearing with self-adjusted load bearing capacity,” 5983781, 1999.
[11] M. Ivantysynova and J. Baker, “Power loss in the lubricating gap between cylinder block and valve plate of swash plate type axial piston machines,” *Int. J. Fluid Power*, vol. 10, no. 2, pp. 29–43, 2009, doi: 10.1080/14399776.2009.10780976.
[12] Reddy; Ivantysyn; Rauschenberger; Weber, “Advanced Micro-Surfacing : Tribological Optimization for Variable Speed Hydraulic Drives,” 2025.
[13] J. Baker and M. Ivantysynova, “Axial sliding bearing and method of reducing power losses therof,” WO 2009/146060 A3, 2009.
[14] S. Ye, H. Tang, Y. Ren, and J. Xiang, “Study on the load-carrying capacity of surface textured slipper bearing of axial piston pump,” *Appl. Math. Model.*, vol. 77, pp. 554–584, 2020, doi: 10.1016/j.apm.2019.07.058.
[15] Z. Wang, L. Sun, B. Han, X. Wang, and Z. Ge, “Study on the Thermohydrodynamic Friction Characteristics of Surface-Textured Valve Plate of Axial Piston Pumps,” *Micromachines*, vol. 13, no. 11, 2022, doi: 10.3390/mi13111891.
[16] A. A. Darbani, L. Shang, J. R. Beale, and M. Ivantysynova, “Slipper surface geometry optimization of the slipper/swashplate interface of swashplate-type axial piston machines,” *Int. J. Fluid Power*, vol. 20, no. 2, pp. 245–270, 2019, doi: 10.13052/ijfp1439-9776.2025.
[17] H. Mo, Y. Hu, and S. Quan, “Thermo-Hydrodynamic Lubrication Analysis of Slipper Pair Considering Wear Profile,” *Lubricants*, vol. 11, no. 5, pp. 1–14, 2023, doi: 10.3390/lubricants11050190.
[18] M. Ernst and A. Vacca, “Hydrostatic vs. hydrodynamic components of fluid pressure in the tribological interfaces of axial piston machines,” *Tribol. Int.*, vol. 157, no. November 2020, p. 106878, 2021, doi: 10.1016/j.triboint.2021.106878.
[19] O. Reynolds, “On the Theory of Lubrication and its Application to Mr. Beauchamp Tower’s Experiments including an Experimental Determination of the Viscosity of Olive Oil.,” *Philos. Trans. R. Soc. London*, vol. 177, pp. 157–234, 1886.
[20] B. J. Hamrock and S. R. Schmid, *Fundamental of Fluid Film Lubrication*. 1991.
[21] Lord Rayleigh, “Notes on the Theory of Lubrication,” *Philosophical Magazine*, vol. 35, pp. 1–12, 1918.
[22] J. M. Bergada and J. Watton, “Axial piston pump slipper balance with multiple lands,” *ASME Int. Mech. Eng. Congr. Expo. Proc.*, pp. 69–73, 2002, doi: 10.1115/IMECE2002-39338.
[23] S. Knoll, “Einfluss der Hydrodynamik auf die Gleitschuhperformance verschiedener meso-strukturierter Gleitschuhe,” TU Dresden, 2025.
[24] M. Ernst and A. Dissertation, “Enabling High-Pressure Operation With Water for the Piston-Cylinder Interface in Axial Piston Machines,” 2021.

Biographies

Svenja Horn received her diploma degree in Aircraft Construction from the Technical University of Dresden in 2018. Since then, she has been working as a research assistant at the Chair of Fluid-Mechatronic Systems, focusing on improving the efficiency and service life of axial piston pumps. Her research concentrates on tribological phenomena at the slipper–swashplate interface, which she investigates using simulations, a hydrostatic tribometer and pump measurements. Furthermore, she applies machine learning algorithms for pump condition monitoring and lifetime prediction.